Machine Learning-Enhanced Visible Light Positioning in IRS-Assisted Indoor Environments with a Single LED Transmitter

Efe Tarhan, *Bilkent University, EEE*

***Abstract*—This research paper explores the use of a single LED transmitter paired with an intelligent mirror array for power-based visible light positioning (VLP) algorithms in a confined space. The study compares the performance of various algorithms in scenarios where the line-of-sight (LoS) path is obstructed, leaving only non-line-of-sight (NLoS) power available for location estimation. To localize the receiver with just one LED transmitter, we conducted multiple measurements at the investigation point using various intelligent reflecting surface (IRS) orientations. The effectiveness of these orientations was evaluated under different channel noise conditions, comparing their root mean squared error (RMSE) values in estimating the location of the visible light communication (VLC) receiver. Our methodology incorporates both classical and machine learning-based algorithms, including Maximum Likelihood Estimation (MLE), K-Nearest Neighbors (KNN) Regression, and Fully Connected Neural Networks (FCNN), to process the power measurements from the mirror arrays. The MLE approach's performance is benchmarked against the Cramer-Rao lower bound to evaluate its precision and reliability. Simulations were conducted to assess the effectiveness of the proposed classical and machine learning-based methods. It was observed that certain IRS orientations, particularly those capable of focusing light on specific room areas, showed enhanced performance in locating the receiver. While the KNN and FCNN algorithms underperformed compared to MLE, they still achieved a level of accuracy influenced by the spatial resolution of their training data. A key advantage of these algorithms is their ability to function without prior knowledge of the channel model, offering increased flexibility in their application.**

***Index Terms* – Intelligent Reflective Surfaces, Mirror Arrays, Visible Light Positioning, Location Estimation, Cramér-Rao Lower Bound, KNN Regression, Fully Connected Neural Networks.**

I. REF—INTRODUCTION

The growing use of light-emitting diodes (LEDs) for interior lighting has spurred academic interest in their alternative applications. LEDs are known for their long lifespan, low energy consumption, and versatile functionality [1]. Their capability for high-frequency operation and rapid switching enables data modulation, thus facilitating communication and positioning applications in indoor environments. This has led to innovative uses of LEDs in indoor visible light positioning (VLP), where numerous studies have proposed position estimation algorithms and explored bounds and limits for localization accuracy [2]–[5].

Received Signal Strength (RSS) is a cost-effective and straightforward method for implementation with LEDs, offering advantages over phase or Time of Arrival (TOA) based estimation algorithms, particularly in terms of accuracy [6]. Additionally, some studies have investigated the hybrid performance of combining RSS with other methods, improving accuracy at the expense of increased computational load [7]. A notable contribution in this field is the development of a generic closed-form expression for the Cramer-Rao Lower Bound (CRLB), which quantifies the accuracy of localization algorithms based on RSS measurements [8].

Intelligent Reflecting Surfaces (IRSs) have introduced novel fields and applications in RF communications and location estimation. An IRS consists of small, low-cost passive elements capable of altering the phase, direction, amplitude, and frequency of RF signals [9]. The authors in [9] provide a comprehensive review of the development of IRS systems. Additionally, IRS has been used for beamforming, enabling the redirection of electromagnetic waves in specific directions, frequencies, or amplitudes. In the study [10], the authors investigate the enhancement of wireless communication via IRS. They propose algorithms for joint active and passive beamforming to optimize signal power at the user, demonstrating significant performance gains in simulated scenarios. In [11], the authors introduce two iterative algorithms for single-user and multi-user scenarios, achieving notable improvements in energy efficiency compared to traditional RIS approaches. Furthermore, several papers delve into the physical properties and channel equations of RIS-based Visible Light Communication (VLC) systems. Abdelhady et al. analyze the light reflection models from RIS elements in metasurface and mirror array-based structures [12]. This research establishes a baseline for further investigation, particularly in point source cases as discussed in [12]. In [13], a low-complexity binary programming algorithm is proposed for maximizing the achievable sum rate. This method significantly enhances the sum rate, especially in scenarios with a large number of users. Lastly, Hanaa Abumarshood et al. present a joint optimization scheme of NOMA decoding order, power allocation, and IRS reflection coefficients to improve the bit error rate (BER) performance of VLC systems using IRS. This approach is particularly effective in scenarios involving blockages and random device orientations [14].

The application of IRSs in wireless positioning systems has also been a focal point of recent studies. There are research in the literature about the usage of multiple IRS under the absence of enough transmitters [15]. Also there are several proposed device-to-device localization schemes for RF communication using RIS receivers [16]–[19].

As traditional methods have become less effective in deciphering complex data, machine learning (ML) techniques have gained prominence in the fields of estimation and prediction. In Visible Light Positioning (VLP), this shift is evident with the adoption of ML approaches for handling complex data through model-free estimation techniques. These ML methods are often referred to as fingerprinting techniques, as they utilize a discrete set of data points collected in a grid pattern within a room. In [20], the authors review current literature on the use of ML as fingerprinting applications in VLP. The paper [21] explores four distinct deep learning architectures, including Fully Connected Neural Networks, Convolutional Neural Networks, and Long Short-Term Memory networks (LSTMs), for two-dimensional location estimation. Haiqi Zhang et al. introduce an innovative high-precision indoor positioning method using visible light and a Deep Neural Network (DNN), optimized by Bayesian regularization in [22]. This approach is notable for its high accuracy achieved with a substantially reduced number of training points and varied data acquisition techniques. Additional works in the literature propose various ML-based approaches for VLP, as seen in [23]–[26]. These studies further demonstrate the versatility and effectiveness of ML techniques in enhancing the accuracy and efficiency of VLP systems.

Despite the numerous contributions to the literature regarding machine learning-based methods and classical approaches for location estimation, there exists a notable gap in sources that comprehensively compare these two domains under similar constraints and conditions. This research aims to bridge this gap by offering key contributions in the following:

- Introducing a study of received power-based position estimation in VLP systems using IRSs, with only a single LED transmitter.
- Proposing a time division multiplexing location estimation scheme, utilizing a single LED transmitter alongside different estimation techniques.
- Comparing the performance of the ML estimator with the CRLB under various channel noise conditions.
- Applying various machine learning-based methods and comparing them with the ML estimator in terms of RMSE.

To support our claims, we have performed simulations using MATLAB to evaluate the effectiveness of the methods we proposed.

The structure of the research paper is as follows: Section II details the channel model for the VLP system in an indoor environment, including essential formulas that describe the relationship between transmitted and received power. In Section III, we introduce our proposed estimation methods, which include the maximum likelihood estimator, KNN regression estimator, and fully connected neural networks. This section also provides the theoretical CRLB for the ML estimator. Section IV describes the simulation setup, including the physical and optical characteristics of the objects in the room and the orientation of the mirrors used in the experiment. The results of the simulations, along with their analysis, are presented in Section V. The paper concludes with final remarks and conclusions in Section VI.

II. CHANNEL PROPERTIES OF VLP WITH INTELLIGENT MIRROR ARRAYS

In the experiment, we utilized a single LED transmitter positioned at the location $\mathbf{l}$, which has a normal vector denoted as $\mathbf{n}$. Both the location and orientation of the LED transmitter are known to the receiver. The transmitter was centrally placed on the ceiling of a room bounded by walls. The VLC receiver was situated at the location $\mathbf{x}$, maintaining a consistent orientation $\overline{\mathbf{n}}$, which was directed straight up throughout the experiment. In addition to the LED and receiver, the setup includes N flat reflective surfaces, denoted as $S_1, S_2, S_3, ..., S_N$, which constitute a controllable intelligent mirror array. This array is positioned on one of the four walls inside the room. Each mirror element is characterized by an orientation vector $\widetilde{\mathbf{n}}_{k,i}$ and position vectors $\widetilde{\mathbf{l}}_{k,i}$, both of which are known to the VLC receiver. The surface area of the mirrors can be calculated by integrating the infinitesimal areas dS_k around the point $\widetilde{\mathbf{l}}_{k,i}$. For the purpose of this study, it is presumed that the mirrors exhibit glossy reflections [27], a key aspect in the formulation of the channel model. Following that, the mirrors are designed to have homogeneous and equal reflection constants across their surfaces, indicated by the constant ρ. The objective is to estimate the location of the receiver, $\mathbf{x}$, by utilizing power measurements derived from light emitted by the LED and subsequently reflected off the mirror surfaces. In a classical setup involving a limited number of LED transmitters and a receiver, at least four transmitters are required to uniquely determine the receiver's location, $\mathbf{x}$, in three-dimensional space. However, in our investigated scenario, where only a single LED transmitter is present in the room, a time-division multiplexing approach is necessary. This involves conducting multiple power measurements with varying orientations of the mirror array, all of which are known to the receiver. The formula for the received power measurement corresponding to the i_{th} orientation of the mirror array can be modeled as follows [28]:

$$P_{RX,i} = P_{TX} H^{LoS}(\mathbf{x}) + P_{TX} \sum_{k=1}^{N} \iint_{S_k} dH^{NLoS}(\mathbf{x}, \widetilde{\mathbf{l}}_{k,i}) + \eta_i \tag{1}$$

The geometric orientation of the components is depicted in Figure 1, where all necessary vectors and components of the VLP environment are defined.

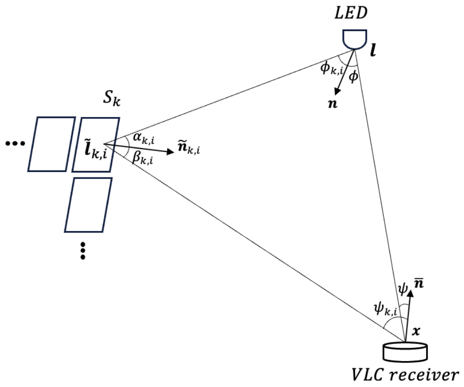

Fig. 1: Schematic representation of the VLP system is illustrated, featuring a single LED and an intelligent reflective array of mirrors, along with a VLC receiver whose location is unknown. The orientation vectors for the LED, mirror S_k, and the VLC receiver are denoted as $\mathbf{n}$, $\widetilde{\mathbf{n}}_{k,i}$, and $\overline{\mathbf{n}}$, respectively. The position vectors of these three entities are represented as $\mathbf{l}$, $\widetilde{\mathbf{l}}_{k,i}$, and $\mathbf{x}$. The schematic also includes the angles of radiance and irradiance between these objects, which are indicated with the variables ψ, ψ_k, ϕ, $\phi_{k,i}$, α, and β.

The received power for the i^{th} orientation of the mirror array is denoted as $P_{RX,i}$, where $i = 1, 2, 3, ..., N_L$. Here, N_L represents the total number of different orientations used to estimate the receiver's location through power measurements. Utilizing various measurements helps eliminate the singularity issue commonly encountered in localization problems. In equation (1), the term H^{LoS} signifies the LoS component of the power received by the VLC receiver. The symbol η_i corresponds to the zero-mean Gaussian noise of $i^t h$ measurement, inherent in the channel, with a noise variance σ that remains consistent and independent [29] across all measurements taken using different mirror array orientations. Following the work done in [12] field-of-view (FOV) of the receiver is presumed to be 90 degrees, attributed to the hemispherical lens mounted on top [30]. The mathematical formulation for the components of the channel gain, is given by the following equations [27]:

$$H^{LoS}(\mathbf{x}) = \frac{(m+1)A(\cos\phi)^m T_s(\psi)g(\psi)\cos\psi}{2\pi\|\mathbf{x}-\mathbf{l}\|^2} \tag{2}$$

and,

$$\begin{aligned} dH^{NLoS}(\mathbf{x}, \widetilde{\mathbf{l}}_k) = {} & (m+1)A(\cos\phi_{k,i})^m \cos\alpha_{k,i} R(\alpha_{k,i}, \beta_{k,i}) \\ & \times \frac{(\cos\psi_{k,i})^m T_s(\psi_{k,i}) g(\psi_{k,i})}{2\pi\|\mathbf{l}-\widetilde{\mathbf{l}}_{k,i}\|^2 \|\mathbf{x}-\widetilde{\mathbf{l}}_{k,i}\|^2} dS_k \end{aligned} \tag{3}$$

where

$$\begin{aligned} R(\alpha_{k,i}, \beta_{k,i}) = {} & \frac{\rho}{2\pi}\big(2r_{k,i}\cos\beta_{k,i} \\ & + (1-r_{k,i})(\mu_{k,i}+1)\cos(\beta_{k,i}-\alpha_{k,i})^{\mu_{k,i}}\big) \end{aligned} \tag{4}$$

In equations (2) and (3), the parameter m represents the Lambertian order of the LED transmitter. This measure of directivity indicates how the visible light source distributes illumination power in a direction deviating by some angle from the source's normal vector. A higher Lambertian order implies that the transmitter is more directional, focusing the emitted power around its normal vector. A denotes the area of the photodetector used in the VLC receiver. The angles ϕ and ψ represent the angles of irradiance and incidence, respectively, on the Line-of-Sight (LoS) path between the transmitter and the receiver. The variables $\phi_{k,i}$, $\psi_{k,i}$, and $\beta_{k,i}$ correspond to the irradiance angles for the k^{th} element of the mirror array, as configured according to the i^{th} known orientation. Each infinitesimal area of a mirror, denoted as dS_k, around the point $\widetilde{\mathbf{l}}$, is treated as a reflective particle. Given that each mirror's dimensions are relatively small compared to the distances between the mirror and the LED, and between the mirror and the receiver, a point source model is adopted for power calculations. This approach leads to the following equality for the power calculations:

$$\begin{aligned} H^{NLoS}(\mathbf{x}, \widetilde{\mathbf{l}}_k) &= \iint_{S_k} dH^{NLoS}(\mathbf{x}, \widetilde{\mathbf{l}}_k) \\ &= (m+1)A(\cos\phi_{k,i})^m \cos\alpha_{k,i} R(\alpha_{k,i}, \beta_{k,i}) \\ &\quad \times \frac{(\cos\psi_{k,i})^m T_s(\psi_{k,i}) g(\psi_{k,i})}{2\pi\|\mathbf{l}-\widetilde{\mathbf{l}}_{k,i}\|^2 \|\mathbf{x}-\widetilde{\mathbf{l}}_{k,i}\|^2} A_{S_k} \end{aligned} \tag{5}$$

The variable A_{S_k} represents the surface area of the k^{th} mirror within the array, which is assumed to be equal for each mirror element. The terms $T_s(\psi)$ and $g(\psi)$ denote the optical filter gain and the optical concentrator gain of the VLC receiver, respectively [28]. As commonly chosen [28], these values are designed to be constant for different incidence angles. To simplify the notation in this research paper, value of $T_s(\psi)g(\psi)$ is set to one. Moreover, the values $r_{k,i}$ and $\mu_{k,i}$ are the fraction of diffuse component and directivity of reflection components respectively [28]. $r_{k,i}$ can take values between 0 and 1 where only the diffuse reflection is considered when it is set to 0. The value of $r_{k,i}$ has been set to 0 in this paper considering direct reflections. The angles mentioned in equations (2), (3), and (4) can be substituted by employing the following equivalent geometric transformations:

$$\cos\phi = \frac{(\mathbf{x}-\mathbf{l})^T\mathbf{n}}{\|\mathbf{x}-\mathbf{l}\|} \tag{6}$$

$$\cos\psi = \frac{(\mathbf{l}-\mathbf{x})^T\overline{\mathbf{n}}}{\|\mathbf{l}-\mathbf{x}\|} \tag{7}$$

$$\cos\phi_{k,i} = \frac{(\widetilde{\mathbf{l}}_{k,i}-\mathbf{l})^T\mathbf{n}}{\|\widetilde{\mathbf{l}}_{k,i}-\mathbf{l}\|} \tag{8}$$

$$\cos\psi_{k,i} = \frac{(\widetilde{\mathbf{l}}_{k,i}-\mathbf{x})^T\overline{\mathbf{n}}}{\|\widetilde{\mathbf{l}}_{k,i}-\mathbf{x}\|} \tag{9}$$

$$\cos\alpha_{k,i} = \frac{(\mathbf{l}-\widetilde{\mathbf{l}}_{k,i})^T\widetilde{\mathbf{n}}_{k,i}}{\|\mathbf{l}-\widetilde{\mathbf{l}}_{k,i}\|} \tag{10}$$

$$\cos\beta_{k,i} = \frac{(\mathbf{x}-\widetilde{\mathbf{l}}_{k,i})^T\widetilde{\mathbf{n}}_{k,i}}{\|\mathbf{x}-\widetilde{\mathbf{l}}_{k,i}\|} \tag{11}$$

By utilizing the given geometric identities and the gain of the receiver, the equations (2) and (3) can be rewritten using vector notation as follows:

$$H^{LoS}(\mathbf{x}) = \frac{(m+1)A((\mathbf{x}-\mathbf{l})^T\mathbf{n})^m(\mathbf{l}-\mathbf{x})^T\bar{\mathbf{n}}}{2\pi\|\mathbf{x}-\mathbf{l}\|^{m+3}} \tag{12}$$

$$\begin{aligned} dH^{NLoS}(\mathbf{x},\widetilde{\mathbf{l}}) = &\frac{(m+1)\big((\widetilde{\mathbf{l}}-\mathbf{l})^T\mathbf{n}\big)\big((\mathbf{l}-\widetilde{\mathbf{l}}_{k,i})^T\widetilde{\mathbf{n}}_{k,i}\big)}{4\pi^2\|\mathbf{l}-\widetilde{\mathbf{l}}_{k,i}\|^{m+3}\|\mathbf{x}-\widetilde{\mathbf{l}}_{k,i}\|^3} \\ &A\rho\big((\widetilde{\mathbf{l}}_{k,i}-\mathbf{x})^T\bar{\mathbf{n}}\big)dS_k\Bigg(2r_{k,i}\frac{(\mathbf{x}-\widetilde{\mathbf{l}}_{k,i})^T\widetilde{\mathbf{n}}_{k,i}}{\|\mathbf{x}-\widetilde{\mathbf{l}}_{k,i}\|} \\ &(1-r_{k,i})(\mu_{k,i}+1)\cos\left(\beta_{k,i}-\alpha_{k,i}\right)^{\mu_{k,i}}\Bigg) \end{aligned} \tag{13}$$

Additionally, the term $\cos\left(\beta_{k,i}-\alpha_{k,i}\right)$ in equation (13) can be calculated as follows:

$$\begin{aligned} \cos\left(\beta_{k,i}-\alpha_{k,i}\right) = &\frac{\big((\mathbf{x}-\widetilde{\mathbf{l}}_{k,i})^T\widetilde{\mathbf{n}}_{k,i}\big)\big((\mathbf{l}-\widetilde{\mathbf{l}}_{k,i})^T\widetilde{\mathbf{n}}_{k,i}\big)}{\|\mathbf{x}-\widetilde{\mathbf{l}}_{k,i}\|\|\mathbf{l}-\widetilde{\mathbf{l}}_{k,i}\|} \\ &+\frac{\|(\mathbf{x}-\widetilde{\mathbf{l}}_{k,i})\times\widetilde{\mathbf{n}}_{k,i}\|\|(\mathbf{l}-\widetilde{\mathbf{l}}_{k,i})\times\widetilde{\mathbf{n}}_{k,i}\|}{\|\mathbf{x}-\widetilde{\mathbf{l}}_{k,i}\|\|\mathbf{l}-\widetilde{\mathbf{l}}_{k,i}\|} \end{aligned} \tag{14}$$

When determining the received power at a given location $\mathbf{x}$, several important factors should be taken into account. Firstly, it is crucial to note that light reflections from the walls are disregarded in this model, as their contribution is typically weaker compared to the power received through the LoS and NLoS paths from the mirrors. Additionally, if feasible, reflections involving more than one mirror element are also excluded, especially in cases where two mirrors face each other at a small angle, leading to significant power loss. For practicality and meaningfulness in the VLC channel detection model, the multipath effect of light is best overlooked. It is also essential to recognize that the equations presented in this chapter are formulated in a generic manner, taking into account general values for the location, orientation, and optical properties of each element within the room's boundaries. The methodology for estimating the location of the VLC receiver, utilizing equations (2) through (14), will be elaborated in the subsequent section. This will include detailed descriptions of the algorithms for applying Maximum Likelihood Estimation and K-Nearest Neighbors methods.

III. VLP USING MLE, KNN AND FCNN TECHNIQUES

For accurate estimation of the receiver's location in 3D space using visible light, relying on a single LED is insufficient to provide a unique solution. Consequently, it necessitates taking multiple measurements with varying orientations of the mirror array. The first method employed for estimating the location of the LED involves a ML estimator. This estimator operates by identifying the most probable coordinates that correspond to the observed power measurements for different mirror orientations. The second method utilizes a machine learning-based KNN regression model. This model predicts the receiver's location by comparing the power measurements at the test location with those of the k-nearest neighbors, which were previously learned by the model during the training phase.

A. ML Estimator

Based on the formula presented in equation (1) for a specific location $\mathbf{x}$, the log-likelihood function corresponding to the received power at the VLC receiver can be expressed as follows:

$$\begin{aligned} \log p(P_{RX}|\mathbf{x}) = \widetilde{a} - \sum_{i=1}^{N_L}\frac{1}{2\sigma_i^2}\Big(&P_{RX,i}-P_{TX}H^{LoS}(\mathbf{x}) \\ &-P_{TX}\sum_{k=1}^{N}\iint_{S_k}dH^{NLoS}(\mathbf{x},\widetilde{\mathbf{l}}_{k,i})\Big)^2 \end{aligned} \tag{15}$$

In the equation, $\widetilde{a}$ represents the constant component of the Gaussian distribution with respect to $\mathbf{x}$, which does not contain any information about the error induced by noise and thus can be minimized. For the localization of the receiver, the ML estimator aims to find the solution $\hat{\mathbf{x}}_{ML}$ that maximizes the log-probability $\log p(P_{RX}|\mathbf{x})$. This corresponds to minimizing the following equation:

$$\begin{aligned} \hat{\mathbf{x}}_{ML} = arg\min_{\mathbf{x}}\sum_{i=1}^{N_L}\frac{1}{\sigma_i^2}\Big(&P_{RX,i}-P_{TX}H^{LoS}(\mathbf{x}) \\ &-P_{TX}\sum_{k=1}^{N}\iint_{S_k}dH^{NLoS}(\mathbf{x},\widetilde{\mathbf{l}}_{k,i})\Big)^2 \end{aligned} \tag{16}$$

B. Estimation with K-Nearest Neighbours (KNN) Regression

KNN regression is a model-free method employed for predicting continuous values corresponding to feature vectors. It operates independently of the need to evaluate equations (12) and (13), which typically provide prior knowledge of the VLP model.

The KNN regression is a fingerprinting-based method where the position estimation is being done by obtaining information from the measurements taken from specific points inside the area of interest [20].

To effectively use KNN regression, a database is required for the evaluation of test data. This database can be constructed by recording power measurements from M distinct points within a pre-selected grid inside the room. At each point, 9 measurements will be taken, and the corresponding position vector will be recorded as the value for that particular vector. The dataset, denoted as $\mathcal{M}$, can be formulated as follows:

$$\mathcal{M} = \left\{\mathbf{x}_n = \begin{bmatrix} P_{RX,1} \\ P_{RX,2} \\ \vdots \\ P_{RX,N_L} \end{bmatrix}, \mathbf{y}_n = \begin{bmatrix} x_1 \\ x_2 \end{bmatrix}, \text{for } \mathbf{n} = 1, 2..., M\right\} \tag{17}$$

Algorithm 1 KNN Regression Algorithm for VLP

```
procedure KNN REGRESSION($\mathcal{M}, P_{RX,test}, k$)
    $distances \leftarrow$ empty list
    for each $\mathbf{x}$ in $\mathcal{M}$ do
        $d \leftarrow \|x_{test} - \mathbf{x}\|$
        Append $(d, x)$ to $distances$
    end for
    Sort $distances$ by distance
    $neighbors \leftarrow$ first $k$ elements of $distances$
    $\hat{x}_{kNN} \leftarrow \frac{1}{k} \sum_{(d,\mathbf{x}) \in neighbors} \mathbf{x}$
    return $\hat{x}_{kNN}$
end procedure
```

The algorithm for implementing KNN regression in the context of VLP is outlined as follows [20]:

Additionally, KNN regression algorithm will be utilized with various datasets, denoted as $\mathcal{M}$, each generated using data measured under conditions of noise with differing variances.

C. Estimation with Fully Connected Neural Network (FCNN)

Neural networks represent a widely used and extensively researched approach for conducting model-free, nonlinear predictions. FCNN stand out as one of the more straightforward methods for training data and making predictions. In FCNN, the output of each neuron is determined by the weights of each input and a bias term, with this output then serving as the input for neurons in the subsequent layer. An example of an FCNN architecture employed for the VLP of the receiver is depicted in Figure 2.

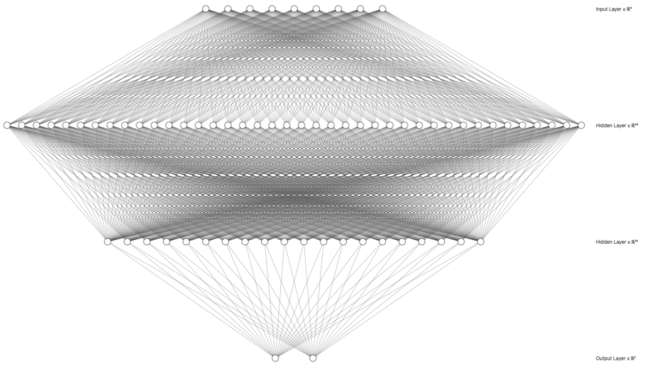

Fig. 2: An example of a neural network used for estimation is as follows: The FCNN is designed with 9 input neurons, corresponding to 9 input power features measured from 9 distinct orientations of the mirror array. It includes two hidden layers, the first with 40 neurons and the second with 20 neurons. The network culminates in two output neurons, which are intended to provide the estimated x and y coordinates of the point in question.

After initializing the models, the dataset $\mathcal{M}$ will be compiled as per the procedure outlined in the algorithm. The features from this dataset will be fed into the input layer of the neural network, which in turn will output the estimated x and y coordinates of the location.

In terms of the neural network architecture, the hyperbolic tangent (tanh) function has been chosen as the activation function between layers. Despite the more common use of the Rectified Linear Unit (ReLU) as a nonlinear activation function, the tanh function is preferred here due to its higher sensitivity to changes in the input features. This heightened sensitivity is attributed to the function's steepness as it approaches the values of 1 and -1 [31]. The tanh function can be mathematically expressed as follows:

$$\phi(x) = \frac{1 - e^{-2x}}{1 + e^{-2x}} \tag{18}$$

For the output layer, the identity function $\phi(x) = x$ has been utilized as the activation function, as this is appropriate for a regression task.

D. Cramér-Rao Lower Bound (CRLB) Calculation for VLP

The CRLB establishes a bound for the variance of an unbiased estimator by employing the Fisher Information Matrix (FIM) [32], denoted as $\mathbf{I}(\mathbf{x})$. The FIM provides a measure of the information that can be gleaned from the transmitters about a given location under estimation, particularly through the effect of the derivative of the location on the channel gain. The FIM can be derived using the partial derivatives of equation (15) as follows:

$$\left[\mathbf{I}(\mathbf{x})\right]_{l_1,l_2} = \sum_{i=1}^{N_L} \frac{P_{TX}^2}{\sigma_i^2} \frac{\partial h_i(\mathbf{x})}{\partial x_{l1}} \frac{\partial h_i(\mathbf{x})}{\partial x_{l2}} \tag{19}$$

For indices $l_1, l_2 = 1, 2, 3$, the total channel gain $h_i(\mathbf{x})$ can be defined as follows, using equation (1):

$$h_i(\mathbf{x}) \triangleq H^{LoS}(\mathbf{x}) + \sum_{k=1}^{N} \iint_{S_k} dH^{NLoS}(\mathbf{x}, \widetilde{\mathbf{l}}_{k,i}) \tag{20}$$

where $P_{RX,i} = P_{TX} h_i(\mathbf{x}) + \eta_i$.

The partial derivative of $h_i(\mathbf{x})$ with respect to x_l can be obtained through the following operation, as detailed in equation (21):

$$\frac{\partial h_i(\mathbf{x})}{\partial x_l} = \frac{\partial H^{LoS}(\mathbf{x})}{\partial x_l} + \sum_{k=1}^{N} \iint_{S_k} \frac{\partial dH^{NLoS}(\mathbf{x}, \widetilde{\mathbf{l}}_{k,i})}{\partial x_l} \tag{21}$$

for $i = 1, 2, ...N_L$ and $l = 1, 2, 3$.

The partial derivatives of the components $H^{LoS}(\mathbf{x})$ and $dH^{NLoS}(\mathbf{x}, \widetilde{\mathbf{l}})$ can be derived using equations (12) through (14) as follows:

$$\begin{aligned} \frac{\partial H^{LoS}(\mathbf{x})}{\partial x_l} &= \frac{(m+1)A}{2\pi \|\mathbf{x} - \mathbf{l}\|^{m+3}} \Big[m n_l \big((\mathbf{x} - \mathbf{l})^T \mathbf{n}\big)^{m-1} \\ &\times \big((\mathbf{l} - \mathbf{x})^T \bar{\mathbf{n}}\big) - \bar{n}_l \big((\mathbf{x} - \mathbf{l})^T \mathbf{n}\big)^m \\ &- \frac{(m+3)(x_l - l_l)\big((\mathbf{x} - \mathbf{l})^T \mathbf{n}\big)^m \big((\mathbf{l} - \mathbf{x})^T \bar{\mathbf{n}}\big)}{\|\mathbf{x} - \mathbf{l}\|^2} \Big] \end{aligned} \tag{22}$$

and,

$$\frac{\partial dH^{NLoS}(\mathbf{x},\widetilde{\mathbf{l}}_{k,i})}{\partial x_l} = \frac{(m+1)A\big((\widetilde{\mathbf{l}}_{k,i}-\mathbf{l})^T\mathbf{n}\big)(\mathbf{l}-\widetilde{\mathbf{l}}_{k,i})^T\widetilde{\mathbf{n}}_{k,i}}{4\pi^2\|\mathbf{l}-\widetilde{\mathbf{l}}_{k,i}\|^{m+3}}$$
$$\rho dS_k\Bigg\{\Bigg[\Big(\widetilde{n}_{k,l,i}(\widetilde{\mathbf{l}}_{k,i}-\mathbf{x})^T\bar{\mathbf{n}}-\bar{n}_l(\mathbf{x}-\widetilde{\mathbf{l}}_{k,i})^T\widetilde{\mathbf{n}}_{k,i}\Big)$$
$$\times\|\mathbf{x}-\widetilde{\mathbf{l}}_{k,i}\|^{-4}-4\|\mathbf{x}-\widetilde{\mathbf{l}}_{k,i}\|^{-6}(x_l-\widetilde{l}_{k,l,i})(\mathbf{x}-\widetilde{\mathbf{l}}_{k,i})^T\widetilde{\mathbf{n}}_{k,i}$$
$$\times(\widetilde{\mathbf{l}}_{k,i}-\mathbf{x})^T\bar{\mathbf{n}}\Bigg]2r_k-(1-r_k)(1+\mu_k)\Bigg[\cos(\beta_{k,i}-\alpha_{k,i})^{\mu_k}$$
$$\times\big(\bar{n}_l\|\mathbf{x}-\widetilde{\mathbf{l}}_{k,i}\|^{-3}+3(\widetilde{\mathbf{l}}_{k,i}-\mathbf{x})^T\bar{\mathbf{n}}\|\mathbf{x}-\widetilde{\mathbf{l}}_{k,i}\|^{-5}(x_l-\widetilde{l}_{k,l,i})\big)$$
$$-\mu_k\cos(\beta_{k,i}-\alpha_{k,i})^{\mu_k-1}\frac{(\widetilde{\mathbf{l}}_{k,i}-\mathbf{x})^T\bar{\mathbf{n}}}{\|\mathbf{x}-\widetilde{\mathbf{l}}_{k,i}\|^3}$$
$$\times\frac{\partial\cos(\beta_{k,i}-\alpha_{k,i})}{\partial x_l}\Bigg]\Bigg\} \tag{23}$$

The partial derivative of $\cos(\beta_{k,i}-\alpha_{k,i})$, as presented in equation 23, can be found as follows:

$$\frac{\partial\cos(\beta_{k,i}-\alpha_{k,i})}{\partial x_l}=\cos\alpha_{k,i}\Big(\widetilde{n}_{k,l,i}\|\mathbf{x}-\widetilde{\mathbf{l}}_{k,i}\|^{-1}$$
$$-(\mathbf{x}-\widetilde{\mathbf{l}}_{k,i})^T\widetilde{\mathbf{n}}_{k,i}\|\mathbf{x}-\widetilde{\mathbf{l}}_{k,i}\|^{-3}(x_l-\widetilde{l}_{k,l,i})\Big)+$$
$$\sin\alpha_{k,i}\Big(\Big\|(\mathbf{x}-\widetilde{\mathbf{l}}_{k,i})\times\widetilde{\mathbf{n}}_{k,i}\Big\|^{-1}\Big\{\widetilde{n}_{k,f(l+1),i}$$
$$\times\big[(x_l-\widetilde{l}_{k,l,i})\widetilde{l}_{k,f(l+1),i}-(x_{f(l+1)}-\widetilde{l}_{k,f(l+1),i})\widetilde{n}_{k,l,i}\big]-$$
$$\widetilde{n}_{k,f(l+2),i}\big[(x_{f(l+2)}-\widetilde{l}_{k,f(l+2),i})\widetilde{n}_{k,l,i}-(x_l-\widetilde{l}_{k,l,i})$$
$$\times\widetilde{n}_{k,f(l+2),i}\big]\Big\}\|\mathbf{x}-\widetilde{\mathbf{l}}_{k,i}\|^{-1}-\|\mathbf{x}-\widetilde{\mathbf{l}}_{k,i}\|^{-3}(x_l-\widetilde{l}_{k,l,i})$$
$$\times\|(\mathbf{x}-\widetilde{\mathbf{l}}_{k,i})\times\widetilde{\mathbf{n}}_{k,i}\|\Big) \tag{24}$$

for $l = 1, 2, 3$, where l denotes the l^{th} components of the given vectors, the function $f(l)$ used in equation (24) can be defined as follows:

$$f(l)=\begin{cases} l & \text{if } l \leq 3, \\ l-3 & \text{otherwise.}\end{cases} \tag{25}$$

The CRLB of the MSE for a generic unbiased estimator can be expressed as follows:

$$E\left\{\|\mathbf{x}-\hat{\mathbf{x}}_{ML}\|^2\right\} \geq CRLB(\mathbf{x}) = trace\left\{\mathbf{I}(\mathbf{x})^{-\mathbf{1}}\right\} \tag{26}$$

In the context of this research, we investigate the performance of estimators under scenarios where the LoS path is obstructed. Consequently, only the NLoS component of the received power is utilized for position estimation. Furthermore, the definition of the channel gain, as delineated in equation 20, along with other related equations, will be modified to exclusively encompass the NLoS channel gain. This modification can be expressed as follows:

$$h_i(\mathbf{x}) \triangleq \sum_{k=1}^{N}\iint_{S_k} dH^{NLoS}(\mathbf{x},\widetilde{\mathbf{l}}_{k,i}) \tag{27}$$

IV. SIMULATION SET-UP

In the simulation setup, we consider a Visible Light Positioning (VLP) design within a room measuring 4 meters in width, 4 meters in length, and 3 meters in height. A single LED transmitter is centrally placed on the ceiling, with its location denoted by $\mathbf{l} = [2, 2, 3]$ meters. The LED's normal vector, $\mathbf{n}$, is oriented towards the center of the mirror array, which is situated in the middle of one of the room's walls. Possible orientations for $\mathbf{n}$ include the vectors $[0, 2, -1.5]$, $[4, 2, -1.5]$, $[2, 0, -1.5]$, and $[2, 4, -1.5]$.

The VLC receiver has an unknown position vector $\mathbf{x}$, which we aim to estimate, and an upwardly directed orientation vector $\bar{\mathbf{n}} = [0, 0, 1]$.

For the simulation, a room bounded by walls serves as the estimation space, with the same dimensions as mentioned earlier. An intelligent mirror array, consisting of 441 individually controllable mirrors $\mathbf{S}_k$ (where $k = 1, 2, 3, ..., 441$), is located in the middle of one wall. Each mirror has its own position $\widetilde{\mathbf{l}}_{k,i}$ and normal $\widetilde{\mathbf{n}}_{k,i}$ vectors. The orientation of these mirrors is adjustable for position estimation purposes. Time Division Multiplexing (TDM) is implemented, with mirrors being rotated by a microcontroller and servo motors along the elevation and azimuth axes. The mirrors undergo 9 or 16 rotations in a sequence agreed upon in the simulation, with the VLC receiver measuring light power at each rotation. Thus, one position estimation cycle encompasses 9 time durations corresponding to the orientation changes of the mirrors.

Additionally, the LED positioned at the room's center has a Lambertian Index (m) of 5, and a power, P_{TX}, of 5 Watts. Each mirror in the array measures 2 cm in height and 4 cm in width, resulting in an 8 cm² area. The mirrors are spaced 2 cm apart horizontally and 1 cm vertically, as shown in Figure 3. The mirrors also possess additional properties: a fraction of the diffuse component r_k, the directivity of reflection μ_k, and a reflection coefficient $\rho_k = 0.95$.

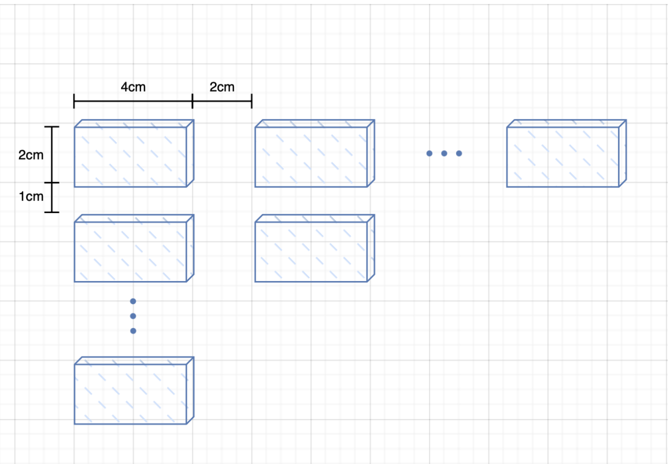

Fig. 3: Arrangement of the mirrors in the intelligent reflective array.

Additionally, the receiver possesses specific properties, such as the Field-of-View (FOV), which is set to 90 degrees, corresponding to 360 steradians. The surface area of the receiver's lens is assumed to be 1cm^2, a realistic size for a photo-detector. The LED transmitter, VLC receiver, and the mirror array have been graphically represented within the room's boundaries using MATLAB, as depicted in Figure 4.

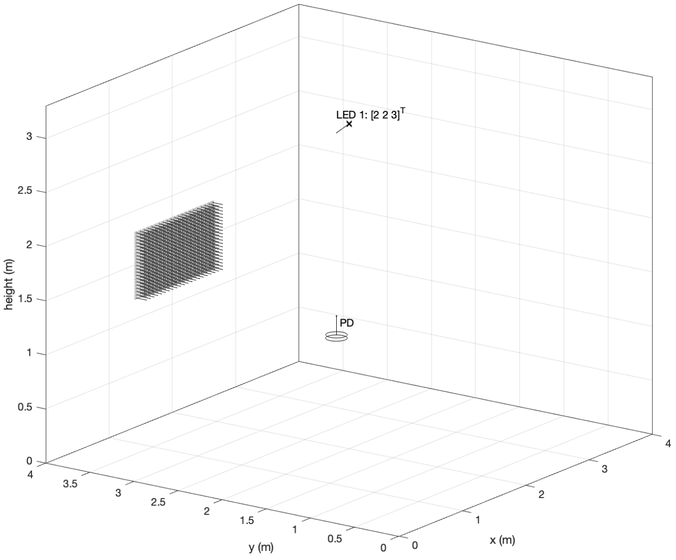

Fig. 4: 3D plot of the room showcasing the LED transmitter, VLC receiver, and mirror array.

For the simulation, three different mirror array orientations were employed: 'directed,' 'random,' and 'uniform.' In the 'directed' orientation, the mirrors' normal vectors were aligned with equally spaced points on a 2D grid, where the grid's height matched that of the receiver. The number of points on this grid was determined based on the desired number of measurements for the estimation task, which were set to 9 or 16. The normal vector for each mirror in the 'directed' array can be defined as follows:

$$\widetilde{\mathbf{n}}_{k,i} = \frac{\widetilde{\mathbf{l}}_{k,i} - \begin{bmatrix} (\frac{4}{\sqrt{m}}+1)(i \mod 4) \\ (\frac{4}{\sqrt{m}}+1)(\lceil \frac{i}{4} \rceil) \\ z \end{bmatrix}}{\left\| \widetilde{\mathbf{l}}_{k,i} - \begin{bmatrix} (\frac{4}{\sqrt{m}}+1)(i \mod 4) \\ (\frac{4}{\sqrt{m}}+1)(\lceil \frac{i}{4} \rceil) \\ z \end{bmatrix} \right\|} \tag{28}$$

for $m \in \{9, 16\}$. z is the height of the receiver and i is the i^{th} power measurement. The value m denotes the number of measurements being taken for each estimation process which can be 9 or 16.

An example orientation of all mirrors in a directed mirror array is illustrated in Figure 5.

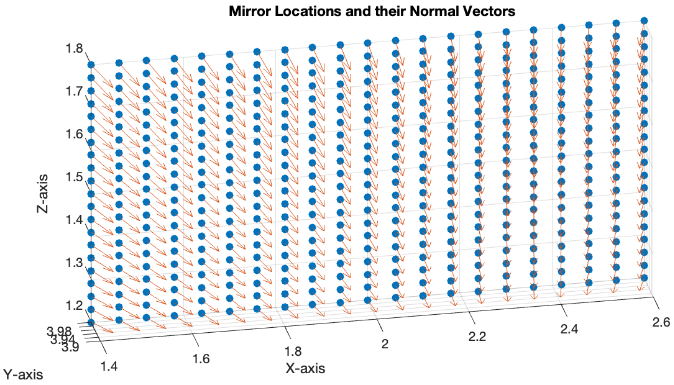

Fig. 5: The mirrors are oriented such that each mirror's normal vector is directed towards the point $[2, 2, 1.5]^T$.

For the "random" orientation scenario, the maximum angles for azimuth and elevation rotations of the mirrors have been set. These maximum angles are chosen to ensure the mirrors can be rotated robustly, precisely, and can accommodate the necessary mechanical systems for the selected angle. In the simulation, the maximum rotation angle is set to $40°$. The rotation is based on the azimuth and elevation angles for each mirror k and each measurement i, with respective distributions $\tilde{\theta} \sim \mathrm{U}[0, 40]$ and $\tilde{\phi} \sim \mathrm{U}[0, 40]$. The normal vector of each mirror in the "random" array can be defined as:

$$\widetilde{\mathbf{n}}_{k,i} = \begin{bmatrix} \cos(\widetilde{\phi})\cos(\widetilde{\theta}) & -\sin(\widetilde{\theta})\cos(\widetilde{\phi}) & \sin(\widetilde{\phi}) \\ \sin(\widetilde{\theta}) & \cos(\widetilde{\theta}) & 0 \\ -\sin(\widetilde{\phi})\cos(\widetilde{\theta}) & \sin(\widetilde{\phi})\sin(\widetilde{\theta}) & \cos(\widetilde{\phi}) \end{bmatrix} \mathbf{n}_0 \tag{29}$$

where $\mathbf{n}_0$ is the normal vector perpendicular and outward to the wall on which the mirror array is mounted.

An example set-up of a mirror array with "random" orientation is depicted in Figure 6.

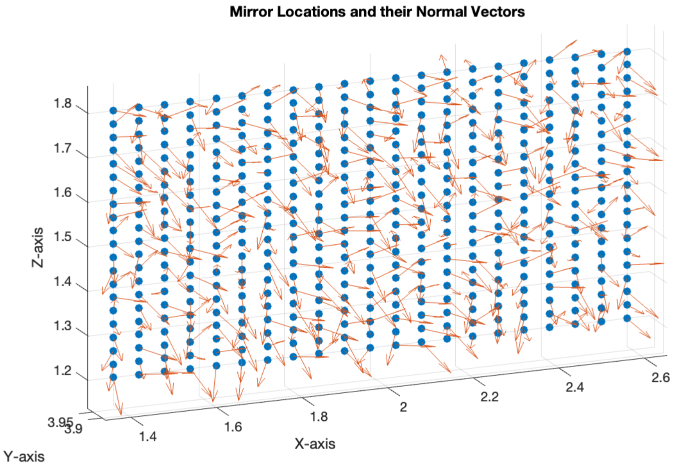

Fig. 6: The mirrors in the 'random' orientation are rotated on the azimuth and elevation angles according to a uniform distribution $\mathrm{U}[0, 40]$ degrees.

Lastly, the mirrors can be 'uniformly' oriented towards a selected direction on the grid. This is achieved by determining the normal vector of the middle mirror in the array to the specified point. This normal vector will then be used as the reference for orienting all mirrors in the array. The normal vector of each mirror in the 'random' array can be defined as:

$$\widetilde{\mathbf{n}}_{k,i} = \frac{\widetilde{\mathbf{l}}_{mid,i} - \begin{bmatrix} (\frac{4}{\sqrt{m}}+1)(\sqrt{i} \mod 4) \\ (\frac{4}{\sqrt{m}}+1)(\lceil \frac{\sqrt{i}}{4} \rceil) \\ z \end{bmatrix}}{\left\| \widetilde{\mathbf{l}}_{mid,i} - \begin{bmatrix} (\frac{4}{\sqrt{m}}+1)(\sqrt{i} \mod 4) \\ (\frac{4}{\sqrt{m}}+1)(\lceil \frac{\sqrt{i}}{4} \rceil) \\ z \end{bmatrix} \right\|} \tag{30}$$

for $m \in \{9, 16\}$ with the addition that $\widetilde{\mathbf{l}}_{\text{mid},i}$ is the location vector of the mirror at the middle of the array. Therefore, the 'uniform' orientation assigns the same normal vector to each mirror as the one used for the mirror at the middle.

An example array design with "uniform" orientation can be seen in Figure 7.

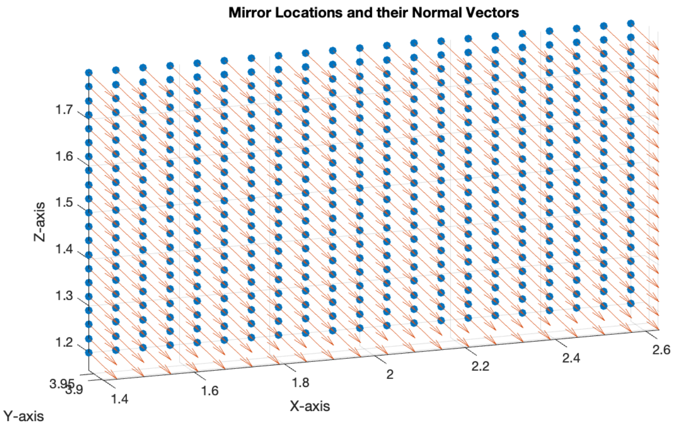

Fig. 7: Orientation of the mirrors in the scenario where they are uniformly directed towards the point $[2.5, 2.5, 0.85]^T$.

These three orientations will be utilized and compared in the simulation part under various algorithms and scenarios.

In the simulation part, the defined methodologies and simulation objects will be employed to obtain results. All power measurements will be taken, including only the NLoS channel gain, assuming the LoS path is obstructed. Initially, power measurements on a cross-section at a specified height will be presented for the three different orientations. Subsequently, the performance of the ML estimator for different noise variances and its comparison with the corresponding CRLBs are compared using plots. Finally, the machine learning-based methods are discussed and compared with the results of the ML estimator.

V. SIMULATION RESULTS AND ANALYSIS

For the simulation part, there are some important remarks to be addressed regarding parameter selections. The transmitted power P_{TX} of the LED is set to 5 Watts, and its location is fixed at $\mathbf{l} = [2, 2, 3]^T$ meters, corresponding to the middle of the ceiling of the room. The center of the intelligent mirror array is positioned at $[2, 4, 1.5]^T$ meters, aligning with the midpoint of one of the walls. The normal vector of the LED is directed towards the midpoint of the mirror array, which corresponds to setting the orientation vector $\mathbf{n} = [0, 0.8, -0.6]^T$ meters. Furthermore, the directivity constant μ_k is set to 5, and the fraction of the diffuse component r_k is set to 0. As mentioned in the simulation section, the dimensions of the mirror array have been chosen to be the same as depicted in Figure 3. After configuring the dimensions of the room, LED transmitter, mirror array, and VLC receiver objects, simulations are conducted to obtain power measurements at a cross-section of the room with a constant height $z = 0.85$ meters.

The results of the power measurements for the randomly oriented mirror array, generated mathematically using the formula in 28, are presented in 2D and 3D plots in Figures 8 and 9.

Fig. 8: 3D NLoS power map of the room obtained using a random mirror orientation. The power has been collected from the cross-section of the room at a height $z = 0.85$ meters.

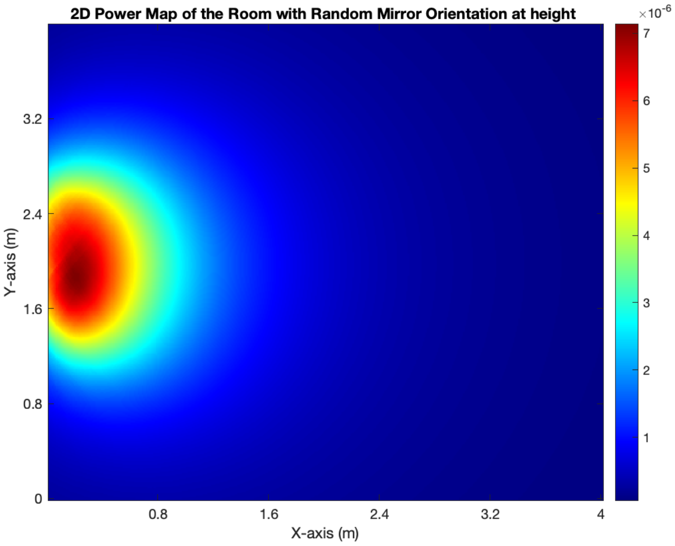

Fig. 9: 2D NLoS power map of the room obtained using a random mirror orientation. The power has been collected from the cross-section of the room at a height $z = 0.85$ meters.

Power measurements using the 'directed' orientation of the mirror array, created using the formula in 27, are presented in 2D and 3D plots in Figures 10 and 11.

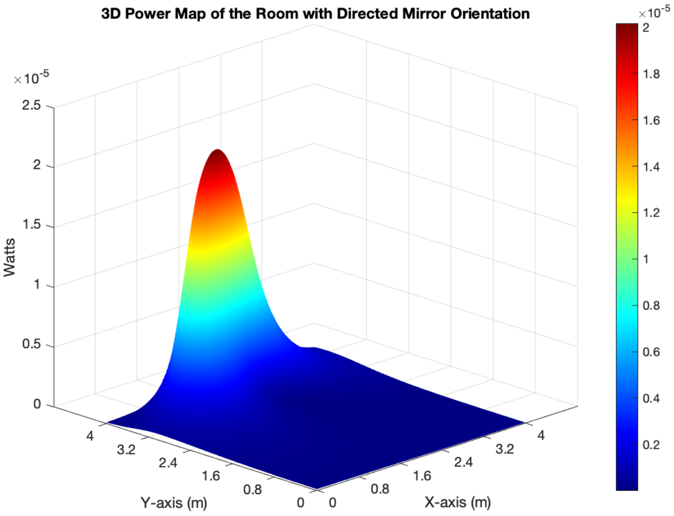

Fig. 10: 3D Non-Line-of-Sight (NLoS) power map of the room obtained using a directed mirror orientation. The point of direction is $[2.5, 2.5, 0.85]^T$. The power has been collected from the cross-section of the room at a height of 0.85 meters.

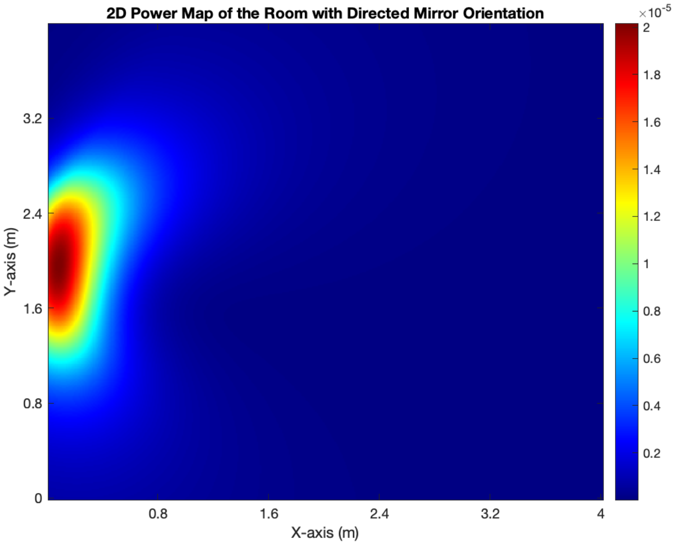

Fig. 11: 2D NLoS power map of the room obtained using a directed mirror orientation. The point of direction is $[2.5, 2.5, 0.85]^T$. The power has been collected from the cross section of the room at height 0.85m

Power measurements using the "uniform" orientation of the mirror array created using the formula in 29 in 2D and 3D plots can be examined from Figures 12 and 13.

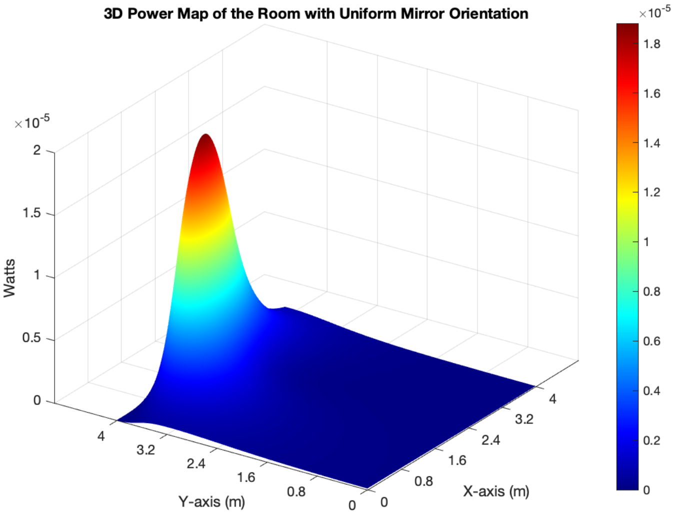

Fig. 12: 3D NLoS power map of the room obtained using a uniform mirror orientation. The point of direction is $[2.5, 2.5, 0.85]^T$. The power has been collected from the cross section of the room at height 0.85m

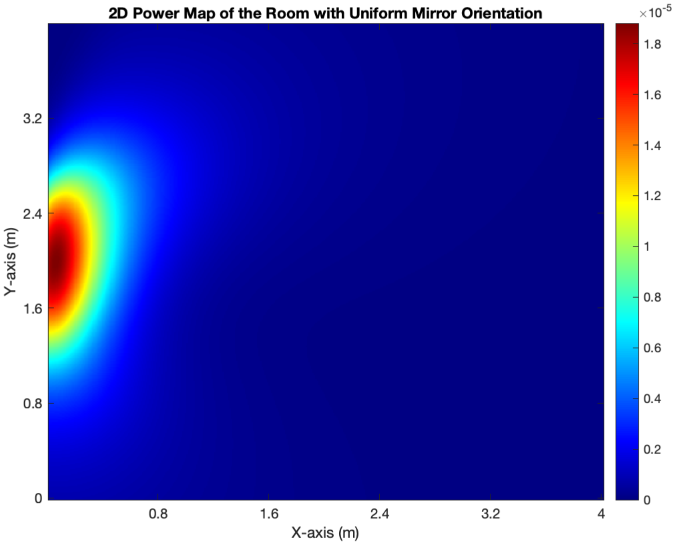

Fig. 13: 2D NLoS power map of the room obtained using a uniform mirror orientation. The point of direction is $[2.5, 2.5, 0.85]^T$. The power has been collected from the cross section of the room at height 0.85m

From the figures, it can be observed that the 'directed' and 'uniform' orientations provide a more focused illumination on the cross-section compared to the 'random' orientation. Although this does not directly imply a correlation with the CRLB and the accuracy of the ML estimator, it can be considered insightful information.

Following the power measurements, the estimation of the VLC receiver's position, located at $[2.5, 2.5, 0.85]^T$ inside the room, has been attempted using a bounded numerical search algorithm. For the algorithm, an initial point $\mathbf{x}_0$ is selected as the starting state, where it iteratively minimizes the difference between the real location and the current state. This is achieved using a model-dependent minimization technique that utilizes the knowledge of equations (12) and (13). The mathematical expression for the initial choice is represented as a random vector below, formulated as:

$$\mathbf{x}_0 = \begin{bmatrix} 2.5 \\ 2.5 \\ 0.85 \end{bmatrix} + \begin{bmatrix} \widetilde{x} \\ \widetilde{y} \\ \widetilde{z} \end{bmatrix} \tag{31}$$

where $\widetilde{x}, \widetilde{y}, \widetilde{z} \sim \mathrm{U}[-0.3, 0.3]$

In the experiment, either 9 or 16 readings are collected at the receiver's location, influenced by AWGN with a noise variance denoted as σ^2. Subsequently, to deduce the position of the VLC receiver, the Levenberg-Marquardt Algorithm, a numerical optimization technique, is applied. This algorithm iteratively refines the initial location vector $\mathbf{x}_0$ to reduce the estimation error. A series of 100 trials were performed for each selected set of σ values, and the resulting Root Mean Square Error (RMSE) was computed. Furthermore, the CRLB was calculated for different mirror orientations, aimed at establishing a minimum threshold for the variance, or experimentally, the RMSE of the unbiased ML estimator. The experiment first focused on the "directed" array orientation, under conditions with either 9 or 16 measurements. The obtained RMSE and CRLB values were documented and are displayed in Figure 14.

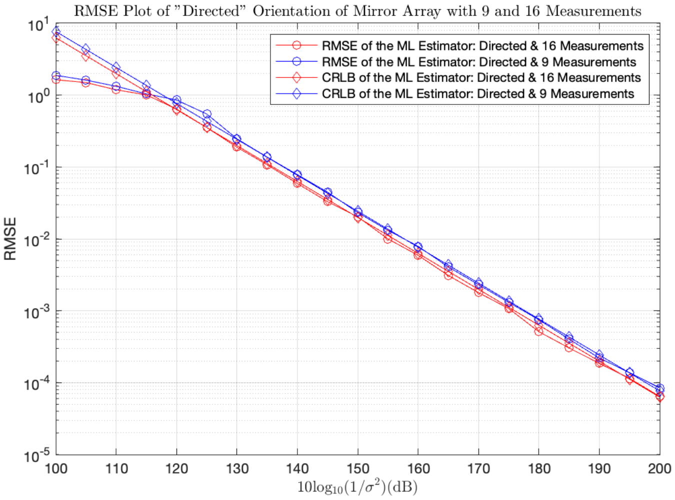

Fig. 14: The RMSE and CRLB values for estimating the location of the VLC receiver across various noise variances, using a "directed" array orientation, are detailed. In these visual representations, the red plots signify estimations conducted with 16 measurements, while the blue plots correspond to estimations made using 9 measurements.

The same experimental procedure has been repeated for the "random" orientation of the mirror array and the results have been recorded to the plot in the Figure 15

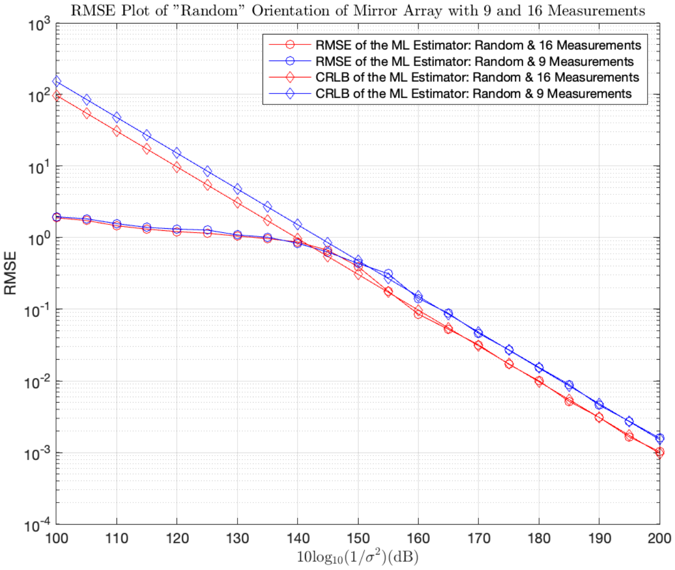

Fig. 15: The RMSE and CRLB values for estimating the location of the VLC receiver across various noise variances, using a "random" array orientation, are detailed. In these visual representations, the red plots signify estimations conducted with 16 measurements, while the blue plots correspond to estimations made using 9 measurements.

Lastly, the results of using a mirror array with "uniform" orientation have been tested and the resultant RMSE and CRLB values are obtained. They can be seen from the plots in Figure 16

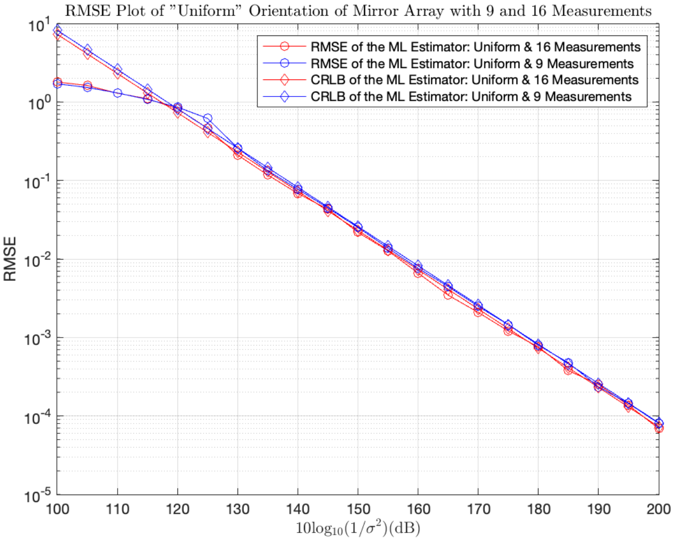

Fig. 16: The RMSE and CRLB values for estimating the location of the VLC receiver across various noise variances, using a "uniform" array orientation, are detailed. In these visual representations, the red plots signify estimations conducted with 16 measurements, while the blue plots correspond to estimations made using 9 measurements.

For the purpose of analyzing and comparing the results, all three figures have been merged into one comprehensive figure, Figure 17, which includes the RMSE and CRLB plots for each of the three orientation schemes.

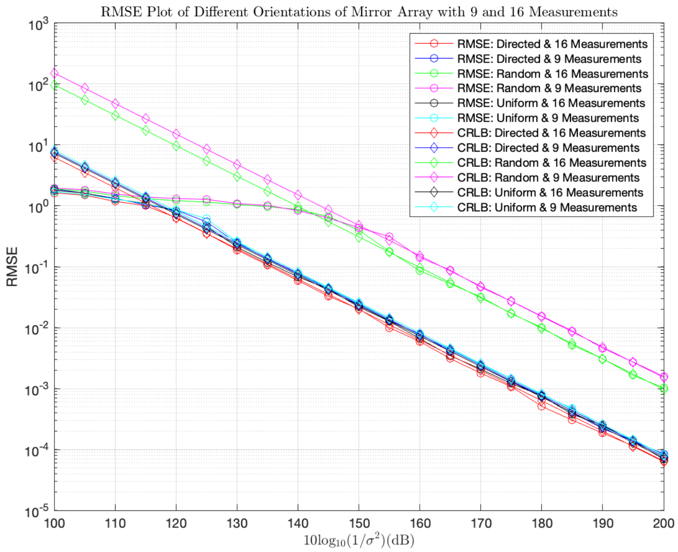

Fig. 17: The plot presents RMSE and CRLB values for estimating the VLC receiver's location across a spectrum of noise variances, using various array orientations.

From Figures 14 - 16, it is evident that the RMSE curves align with their respective CRLB curves as the Signal-to-Noise Ratio (SNR) increases, coinciding with a decrease in the channel noise variance σ. This alignment is anticipated, given that the CRLB delineates the minimum variance achievable by any unbiased estimator.

Figure 17 reveals that in comparison to the ”random” orientation, both ”directed” and ”uniform” orientations demonstrate superior performance. This improvement is attributed to the enhanced focusability of light in the ”directed” and ”uniform” scenarios, which are more sensitive to the position vector. Notably, the ”directed” orientation slightly outperforms the ”uniform” orientation in terms of estimation accuracy.

Furthermore, due to the room's physical boundaries and the numerical optimizer's operation within specified limits, the RMSE curve falls below the CRLB curve at lower noise variances. This is because the estimator is confined within the room's dimensions, whereas the CRLB presupposes an unbounded estimation environment, allowing for an RMSE that is lower than the CRLB under certain conditions.

Subsequent to the ML estimator's results, the KNN regression model was applied. Following the approach outlined in KNN regression algorithm, the algorithm estimated the location of the VLC receiver independently of any model knowledge. This estimation process was repeated by generating training datasets for various noise variances and evaluating them against a test set with a uniform noise variance. The test set comprised 500 randomly chosen data points on the cross-section at $z = 0.85$ m, following a uniform distribution with $x, y \sim \mathrm{U}(0, 4)$. The outcomes of the KNN regression, tested with datasets created at noise variances $\sigma^2 = 10^{-10}, 10^{-14}, 10^{-18}$, are depicted in Figures 18, 19, and 20, showcasing the effects of varying the hyperparameter for the number of nearest neighbours.

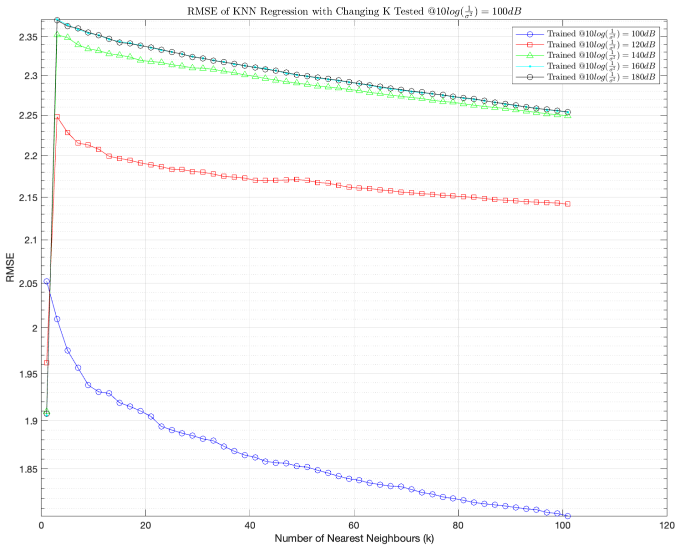

Fig. 18: The RMSE values for the KNN regression model, relative to a spectrum of 'number of nearest neighbours' values, are documented. This model was trained using data produced under various noise variances and tested against data generated under a noise condition with $\sigma^2 = 10^{-10}$.

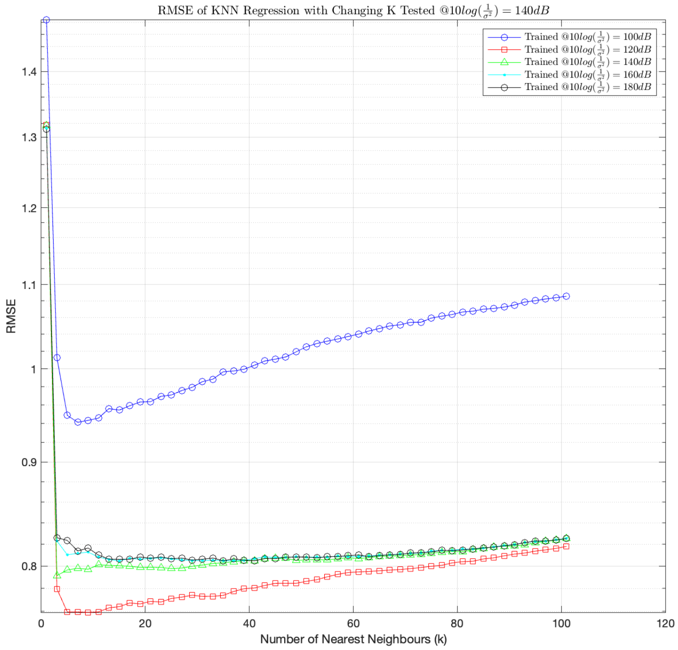

Fig. 19: The RMSE values for the KNN regression model, relative to a spectrum of 'number of nearest neighbours' values, are documented. This model was trained using data produced under various noise variances and tested against data generated under a noise condition with $\sigma^2 = 10^{-14}$.

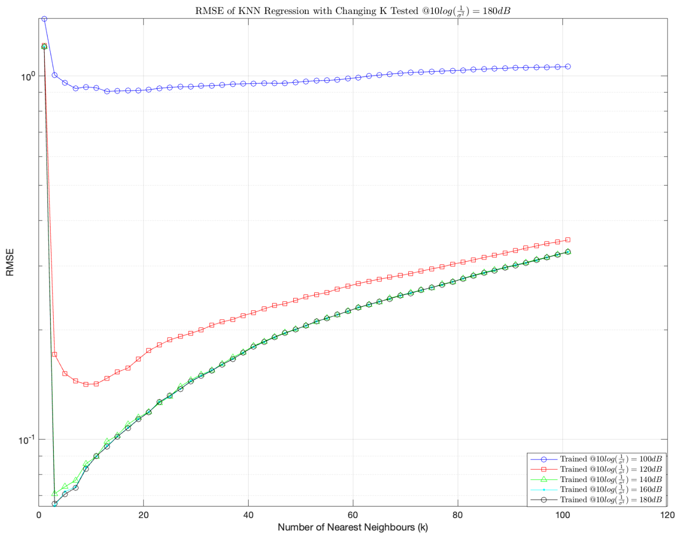

Fig. 20: The RMSE values for the KNN regression model, relative to a spectrum of 'number of nearest neighbours' values, are documented. This model was trained using data produced under various noise variances and tested against data generated under a noise condition with $\sigma^2 = 10^{-18}$.

In the estimation experiments with test data generated under noise variances of $\sigma^2 = 10^{-14}$ and $\sigma^2 = 10^{-18}$, the RMSE worsens as the number of neighbours increases. Optimal performance for these two models is observed when using 3-4 neighbours as the hyperparameter. Interestingly, compared to the Maximum Likelihood (ML) estimator, the model trained with the lowest noise variance dataset does not always yield the lowest RMSE, indicating that each training set may perform differently on various test sets.

Contrastingly, in the first experiment shown in Figure 18, which uses a test set generated under a noise variance of $\sigma^2 = 10^{-10}$, the model's performance improves with an increasing number of neighbours across all five cases. However, a closer inspection of the RMSE values reveals minimal variation, suggesting a convergence beyond a certain point. This pattern could be attributed to the VLC receiver's location being closer to the room's center, where increasing the number of neighbours may lead to predictions gravitating towards the room's central area, especially in high noise variance situations.

Lastly, various FCNN models have been explored to estimate the location of the VLC receiver. Networks with 0, 1, 2, and 3 hidden layers were trained using data generated under noise variances of $\sigma^2 = 10^{-10}$ and $\sigma^2 = 10^{-14}$. The resulting RMSE values from these models were then compared with those from the previously mentioned KNN regression. The comparative results of the FCNN and KNN models are displayed in Figures 21 and 22.

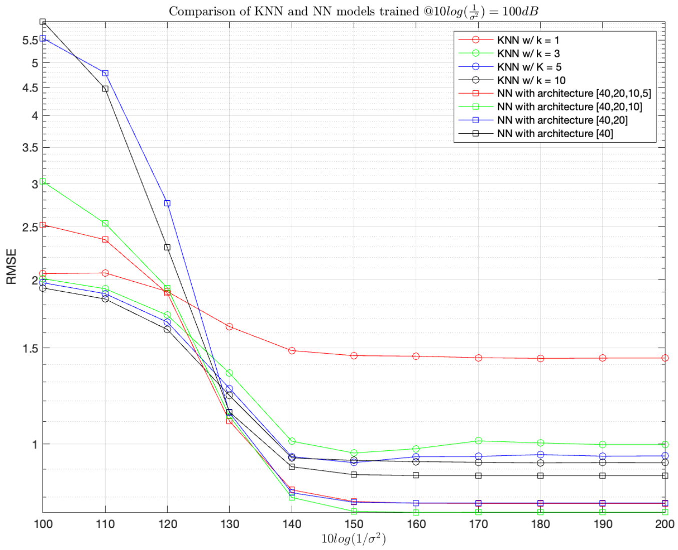

Fig. 21: The RMSE performances of the estimation models, employing both FCNN and KNN algorithms, are evaluated for different noise variances. These models are trained using a dataset generated under a noise variance of $\sigma^2 = 10^{-10}$.

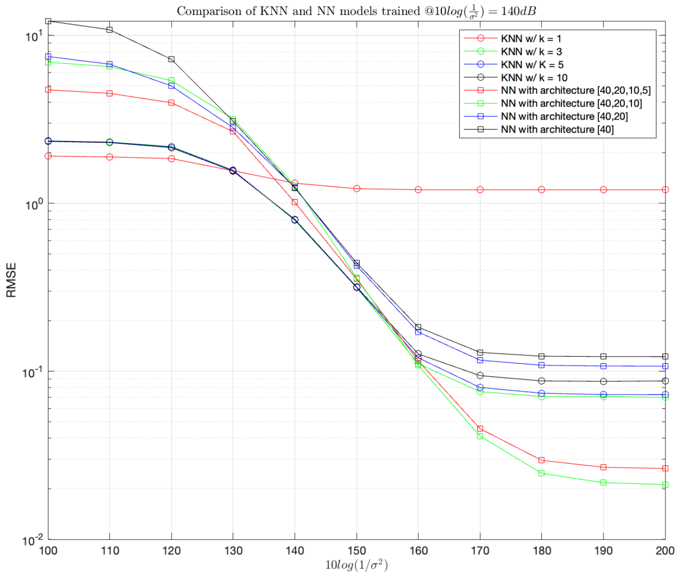

Fig. 22: The RMSE performances of the estimation models, employing both FCNN and KNN algorithms, are evaluated for different noise variances. These models are trained using a dataset generated under a noise variance of $\sigma^2 = 10^{-14}$.

Compared to the KNN models, it is observed that the FCNN architectures exhibit superior performance at higher noise variances. This is attributed to the SNR levels being sufficiently high to capture the essence of the data. By varying the neural network architectures and adjusting hyperparameters, further enhancements in estimation accuracy can be achieved. While the machine learning-based models may not perform as well as the classical ML estimation under certain conditions, they demonstrate commendable estimation capabilities, particularly under high SNR scenarios, even without explicit knowledge of the underlying model. Additionally, their performance can be improved by enlarging the dataset, which involves increasing the number of points where power measurements are collected.

VI. CONCLUDING REMARKS

In this research paper, we investigate the VLP performances of the ML estimator, KNN regression, and various FCNN architectures under different SNR conditions. Throughout the study, the LoS path is assumed to be blocked, allowing us to assess the performance of the estimators in scenarios where no LoS light power reaches the VLC receiver. These models were tested in a simulated environment featuring a single LED transmitter and an intelligent mirror array. This research aims to demonstrate that position estimation can be effectively achieved using only one light source, with the assistance of a mirror array to overcome the challenges of singularity. In the classical ML estimation approach, it has been observed that directing the mirrors to various points inside the room improves power measurement and, consequently, the estimation performance. Additionally, a model-free KNN regression algorithm has been employed for location estimation, alongside classical estimation methods. The results indicate that these models perform well under the influence of AWGN with low variance. To compare the KNN with another machine learning-based method, various FCNN structures were tested under different noise conditions. Notably, the neural networks demonstrated superior performance compared to KNN regression, particularly under high channel SNR conditions, where they could estimate the location of the receiver with an RMSE of 0.1 times the resolution of the power measurements. Overall, this paper shows that employing multiple measurements and machine learning-based methods can achieve cost-effective estimation, albeit with a trade-off in estimation performance.

REFERENCES

[1] M. Yoshino, S. Haruyama, and M. Nakagawa, "High-accuracy positioning system using visible LED lights and image sensor," in *2008 IEEE Radio and Wireless Symposium*, 2008, pp. 439–442.

[2] J. Luo, L. Fan, and H. Li, "Indoor positioning systems based on visible light communication: State of the art," *IEEE Communications Surveys & Tutorials*, vol. 19, no. 4, pp. 2871–2893, 4th Quart. 2017.

[3] M. F. Keskin, A. D. Sezer, and S. Gezici, "Localization via visible light systems," *Proceedings of the IEEE*, vol. 106, no. 6, pp. 1063–1088, June 2018.

[4] J. Armstrong, Y. Sekercioglu, and A. Neild, "Visible light positioning: A roadmap for international standardization," *IEEE Communications Magazine*, vol. 51, no. 12, pp. 68–73, Dec. 2013.

[5] H. Steendam, T. Q. Wang, and J. Armstrong, "Theoretical lower bound for indoor visible light positioning using received signal strength measurements and an aperture-based receiver," *Journal of Lightwave Technology*, vol. 35, no. 2, pp. 309–319, Jan 2017.

[6] A. Hatami and K. Pahlavan, "Performance comparison of rss and toa indoor geolocation based on uwb measurement of channel characteristics," in *2006 IEEE 17th International Symposium on Personal, Indoor and Mobile Radio Communications*, 2006, pp. 1–6.

[7] H. Ge, F. Jiang, and Z. Zhang, "A hybrid localization algorithm of rss and toa based on an ensembled neural network," in *2019 IEEE 8th Joint International Information Technology and Artificial Intelligence Conference (ITAIC)*, 2019, pp. 1280–1284.

[8] B. Zhou, A. Liu, and V. Lau, "On the fundamental performance limit of visible light-based positioning," in *13th International Conference on Signal Processing and Communication Systems (ICSPCS)*, 2019, pp. 1–6.

[9] E. Basar, M. Di Renzo, J. De Rosny, M. Debbah, M.-S. Alouini, and R. Zhang, "Wireless communications through reconfigurable intelligent surfaces," *IEEE Access*, vol. 7, pp. 116 753–116 773, 2019.

[10] Q. Wu and R. Zhang, "Intelligent reflecting surface enhanced wireless network via joint active and passive beamforming," *IEEE Transactions on Wireless Communications*, vol. 18, no. 11, pp. 5394–5409, 2019.

[11] T. Ma, Y. Xiao, X. Lei, W. Xiong, and M. Xiao, "Distributed reconfigurable intelligent surfaces assisted indoor positioning," *IEEE Transactions on Wireless Communications*, vol. 22, no. 1, pp. 47–58, 2023.

[12] A. M. Abdelhady, A. K. S. Salem, O. Amin, B. Shihada, and M.-S. Alouini, "Visible light communications via intelligent reflecting surfaces: Metasurfaces vs mirror arrays," *IEEE Open Journal of the Communications Society*, vol. 2, pp. 1–20, 2021.

[13] S. Sun, F. Yang, and J. Song, "Sum rate maximization for intelligent reflecting surface-aided visible light communications," *IEEE Communications Letters*, vol. 25, no. 11, pp. 3619–3623, 2021.

[14] H. Abumarshoud, B. Selim, M. Tatipamula, and H. Haas, "Intelligent reflecting surfaces for enhanced noma-based visible light communications," in *ICC 2022 - IEEE International Conference on Communications*, 2022, pp. 571–576.

[15] A. Nasri, A. H. A. Bafghi, and M. Nasiri-Kenari, "Wireless localization in the presence of intelligent reflecting surface," *IEEE Wireless Communications Letters*, vol. 11, no. 7, pp. 1315–1319, 2022.

[16] M. Ammous and S. Valaee, "Cooperative positioning with the aid of reconfigurable intelligent surfaces and zero access points," in *2022 IEEE 96th Vehicular Technology Conference (VTC2022-Fall)*, 2022, pp. 1–5.

[17] Y. Liu, E. Liu, R. Wang, and Y. Geng, "Reconfigurable intelligent surface aided wireless localization," in *ICC 2021 - IEEE International Conference on Communications*, 2021, pp. 1–6.

[18] N. Afzali, M. J. Omidi, K. Navaie, and N. S. Moayedian, "Low complexity multi-user indoor localization using reconfigurable intelligent surface," in *2022 30th International Conference on Electrical Engineering (ICEE)*, 2022, pp. 731–736.

[19] T. Zhou, K. Xu, Z. Shen, W. Xie, D. Zhang, and J. Xu, "Aoa-based positioning for aerial intelligent reflecting surface-aided wireless communications: An angle-domain approach," *IEEE Wireless Communications Letters*, vol. 11, no. 4, pp. 761–765, 2022.

[20] H. Q. Tran and C. Ha, "Machine learning in indoor visible light positioning systems: A review," *Neurocomputing*, vol. 491, pp. 117–131, 2022. [Online]. Available: https://www.sciencedirect.com/science/article/pii/S092523122200306X

[21] X. Lin and L. Zhang, "Intelligent and practical deep learning aided positioning design for visible light communication receivers," *IEEE Communications Letters*, vol. 24, no. 3, pp. 577–580, 2020.

[22] H. Zhang, J. Cui, L. Feng, A. Yang, H. Lv, B. Lin, and H. Huang, "High-precision indoor visible light positioning using deep neural network based on the bayesian regularization with sparse training point," *IEEE Photonics Journal*, vol. 11, no. 3, pp. 1–10, 2019.

[23] X. Guo, S. Shao, N. Ansari, and A. Khreishah, "Indoor localization using visible light via fusion of multiple classifiers," *IEEE Photonics Journal*, vol. 9, no. 6, pp. 1–16, 2017.

[24] V. P. Rekkas, L. A. Iliadis, S. P. Sotiroudis, A. D. Boursianis, P. Sarigiannidis, D. Plets, W. Joseph, S. Wan, C. G. Christodoulou, G. K. Karagiannidis, and S. K. Goudos, "Artificial intelligence in visible light positioning for indoor iot: A methodological review," *IEEE Open Journal of the Communications Society*, vol. 4, pp. 2838–2869, 2023.

[25] M. Xu, W. Xia, Z. Jia, Y. Zhu, and L. Shen, "A vlc-based 3-d indoor positioning system using fingerprinting and k-nearest neighbor," in *2017 IEEE 85th Vehicular Technology Conference (VTC Spring)*, 2017, pp. 1–5.

[26] M. Saadi, T. Ahmad, Y. Zhao, and L. Wuttisttikulkij, "An led based indoor localization system using k-means clustering," in *2016 15th IEEE International Conference on Machine Learning and Applications (ICMLA)*, 2016, pp. 246–252.

[27] O. Gonzalez, S. Rodriguez, R. Perez-Jimenez, B. Mendoza, and A. Ayala, "Error analysis of the simulated impulse response on indoor wireless optical channels using a Monte Carlo-based ray-tracing algorithm," *IEEE Transactions on Communications*, vol. 53, no. 1, pp. 124–130, 2005.

[28] T. Komine and M. Nakagawa, "Fundamental analysis for visible-light communication system using LED lights," *IEEE Transactions on Consumer Electronics*, vol. 50, no. 1, pp. 100–107, Feb. 2004.

[29] M. F. Keskin, E. Gonendik, and S. Gezici, "Improved lower bounds for ranging in synchronous visible light positioning systems," *Journal of Lightwave Technology*, vol. 34, no. 23, pp. 5496–5504, Dec 2016.

[30] J. Barry, J. Kahn, W. Krause, E. Lee, and D. Messerschmitt, "Simulation of multipath impulse response for indoor wireless optical channels," *IEEE Journal on Selected Areas in Communications*, vol. 11, no. 3, pp. 367–379, Apr. 1993.

[31] S.-L. Shen, N. Zhang, A. Zhou, and Z.-Y. Yin, "Enhancement of neural networks with an alternative activation function tanhlu," *Expert Systems with Applications*, vol. 199, p. 117181, 2022. [Online]. Available: https://www.sciencedirect.com/science/article/pii/S0957417422005681

[32] H. V. Poor, *An Introduction to Signal Detection and Estimation*. New York: Springer-Verlag, 1994.